Magnetic and singlet phases in the three-dimensional periodic Anderson Model

Wiliam S. Oliveira,[1] Thereza Paiva,[1] Richard T. Scalettar,[2] and Natanael C. Costa[1]
[1]*Instituto de Física, Universidade Federal do Rio de Janeiro, Caixa Postal 68.528, 21941-972 Rio de Janeiro, Rio de Janeiro, Brazil*
[2]*Department of Physics and Astronomy, University of California, Davis, California 95616, USA*

(Received 20 March 2023; accepted 31 August 2023; published 11 September 2023)

Heavy-fermion materials are compounds in which localized f orbitals hybridize with delocalized d ones, leading to quasiparticles with large renormalized masses. The presence of strongly correlated f electrons at the Fermi level may also lead to long-range order, such as magnetism, or unconventional superconductivity. From a theoretical point of view, the "standard model" for heavy-fermion compounds is the periodic Anderson model (PAM). Despite being extensively scrutinized, its thermodynamic properties in three-dimensional (3D) lattices have not been carefully addressed by unbiased methodologies. Here we investigate the 3D PAM employing state-of-the-art finite-temperature auxiliary-field quantum Monte Carlo simulations. We present the behavior of the kinetic energy, the entropy, the specific heat, and the double occupancy as functions of the temperature and the hybridization strength. From these quantities, and by the analysis of the spin-spin correlation functions, we investigate the occurrence of magnetic phase transitions at finite temperatures, and we determine the phase diagram of the model, including the behavior of the Néel temperature as a function of the external parameters.

DOI: 10.1103/PhysRevB.108.115121

I. INTRODUCTION

Real-space quantum Monte Carlo (QMC) studies of itinerant electron and electron-phonon models, such as the Hubbard, Holstein, Su-Schrieffer-Heeger (SSH), and periodic Anderson Hamiltonians, have often focused on one and two dimensions [1–4]. In the case of the Hubbard model, this choice is partly driven by direct implications in quasi-two-dimensional compounds, e.g., layered geometries relevant to cuprate materials and d-wave superconductivity [5]. Similarly, other two-dimensional (2D) materials and lattices, such as graphene and transition metal dichalcogenides, may exhibit interesting topological properties or long-range-ordered phases [6,7]. However, the choice of lower dimensional lattices is also a practical one: with the system sizes limited to $\mathcal{O}(10^2$–$10^3)$ sites, reliable finite-size scaling analysis becomes challenging in three-dimensional (3D) geometries. Unfortunately, due to the Mermin-Wagner theorem, a lower dimension may also lead to restrictions for the occurrence of long-range-ordered phases. This is the case of Hubbard-like models, which at half-filling any possible long-range antiferromagnetic phase should occur only at zero temperature [8]. Studies within dynamical mean-field theory (DMFT), dynamical cluster approximation, or diagrammatic Monte Carlo avoid this issue, while introducing other approximations or limitations.

A significant exception is the great numerical effort devoted to investigating the 3D (cubic) Hubbard [9–12] model, the 3D (cubic) Holstein [13] model, and the 3D (cubic perovskite) SSH model [14] within QMC simulations. These studies have established quantitatively the dependence of their critical temperatures at half-filling—T_N (Néel) for the Hubbard model and T_{cdw} (CDW) for the Holstein model. Such a difficult task is alleviated by the increasing computational resources, with parallelization protocols, as well as the development of new methodologies (e.g., machine learning or Langevin accelerations). Although this leap to 3D geometries is a significant accomplishment, so far it has been carried out mostly for single-band models.

As a paradigm for two-band systems, the periodic Anderson model (PAM) considers the interplay of localized and itinerant fermions. Unlike the half-filled 3D Hubbard model, where one has a ground state antiferromagnetic phase even for $U_f/t \to 0$, in the PAM there is a finite critical ratio of interband to conduction electron hybridization V/t, separating antiferromagnetic and singlet phases at $T = 0$. Thus, one has a substantially more rich phase diagram. The Fermi surface of the cubic lattice with nearest-neighbor hoppings exhibits perfect nesting at half-filling, for $\mathbf{q} = (\pi, \pi\,\pi)$. Such a characteristic leads to instabilities for this wave vector, which, in turn, may favor an insulating antiferromagnetic state at small hybridizations.

However, its quantitative critical boundaries have not been determined by unbiased methodologies at the present moment. Early attempts to describe the properties of the 3D PAM by QMC were performed in Refs. [15–17], in which the behavior of the spin-spin correlation functions was examined for different values of V/t and U_f/t, but for small lattices and without a finite-size scaling analysis. The main goal of this paper is to bridge this gap by extending work on real-space QMC in three dimensions to the PAM and comparing it with the well-known 2D case.

As the standard model for heavy-fermion compounds, the study of the 3D PAM is a significant step towards understanding the thermodynamic properties of these materials [18]. In particular, the application of pressure changes the conduction electron bandwidth $W = 12\,t$ and the hybridization V between localized and conduction bands (with a lesser

effect on on-site repulsion). These changes affect the nature of both high- and low-temperature responses, from the transition temperatures to transport properties. Identifying these energy scales is crucial since, given a density-functional theory parametrization of W and V, our phase transitions can be used for quantitative benchmarking of heavy-fermion properties—such as the cerium volume collapse transition [19]. The present paper is organized as follows. In Sec. II we present the periodic Anderson model and highlight the main features of the QMC method together with the quantities of interest. Our results are presented in Sec. III, and the main conclusions are summarized in Sec. IV.

II. MODEL AND METHOD

The PAM Hamiltonian reads

$$\hat{\mathcal{H}} = -t \sum_{\langle \mathbf{i},\mathbf{j}\rangle,\sigma} (d^\dagger_{\mathbf{i}\sigma} d_{\mathbf{j}\sigma} + \text{H.c.}) - V \sum_{\mathbf{i},\sigma} (d^\dagger_{\mathbf{i}\sigma} f_{\mathbf{i}\sigma} + \text{H.c.}) - \mu \sum_{\mathbf{i},\sigma,\alpha} n^\alpha_{\mathbf{i}\sigma} + U_f \sum_{\mathbf{i}} \left(n^f_{\mathbf{i}\uparrow} - \frac{1}{2}\right)\left(n^f_{\mathbf{i}\downarrow} - \frac{1}{2}\right), \quad (1)$$

where the sums run over a three-dimensional simple cubic lattice, with $\langle \mathbf{i}, \mathbf{j}\rangle$ denoting nearest-neighbor sites, and $\alpha = d$ or f. The first term on the right-hand side of Eq. (1) corresponds to the hopping of conduction d electrons, while the last one describes the Coulomb repulsion on localized f orbitals. The hybridization between these two orbitals is given by an on-site interorbital hopping V, the chemical potential, and the f-electron site energy $\mu = E_f = 0$, and both bands are individually half-filled. Hereafter, we set the energy scale as being units of the hopping integral t and we define $U_f/t = 6$.

We investigate the thermodynamic properties of the 3D PAM by performing finite-temperature auxiliary-field QMC simulations, namely, determinant QMC [20–22]. The DQMC method is an unbiased technique commonly used to investigate tight-binding Hamiltonians: it maps a d-dimensional interacting system to a noninteracting $(d+1)$-dimensional one, with the additional imaginary-time coordinate $0 \leqslant \tau \leqslant \beta$, where β is the inverse temperature. Within this approach, one separates the one-body ($\hat{\mathcal{K}}$) and two-body ($\hat{\mathcal{P}}$) pieces in the partition function by using the Trotter-Suzuki decomposition, i.e., by defining $\beta = L_\tau \Delta\tau$, with L_τ being the number of imaginary-time slices and $\Delta\tau$ being the discretization grid. Then,

$$\mathcal{Z} = \text{Tr} e^{-\beta\hat{\mathcal{H}}} = \text{Tr}\left[\left(e^{-\Delta\tau(\hat{\mathcal{K}}+\hat{\mathcal{P}})}\right)^{L_\tau}\right] \approx \text{Tr}\left[e^{-\Delta\tau\hat{\mathcal{K}}} e^{-\Delta\tau\hat{\mathcal{P}}} e^{-\Delta\tau\hat{\mathcal{K}}} e^{-\Delta\tau\hat{\mathcal{P}}} \cdots\right], \quad (2)$$

with an error proportional to $(\Delta\tau)^2$, but being exact in the limit $\Delta\tau \to 0$. The resulting partition function is rewritten in quadratic (single-body) form through a discrete Hubbard-Stratonovich transformation (HST) on the two-body terms, $e^{-\Delta\tau\hat{\mathcal{P}}}$. This HST introduces discrete auxiliary fields with components on each of the space and imaginary-time lattice coordinates, which are sampled by Monte Carlo techniques. In this work we choose $\Delta\tau = 0.1$, so that the error from the Trotter-Suzuki decomposition is less than, or comparable to, statistical errors from the Monte Carlo sampling. More details about the method are discussed in Refs. [23–25] and references therein. Although DQMC is unbiased, its low-temperature application is restricted to systems with particle-hole or other symmetries, owing to the minus-sign problem [26–28]. For this reason, our focus is on half-filling, $\mu = 0$, where the sign problem is absent.

In order to examine signatures for the formation of local moments and antiferromagnetic long-range order, we first investigate the thermodynamic properties, namely, the internal energy and specific heat per site,

$$e(T) = \frac{1}{N}\langle\hat{\mathcal{H}}\rangle, \quad (3)$$

$$c(T) = \frac{1}{N}\frac{d\langle\hat{\mathcal{H}}\rangle}{dT}, \quad (4)$$

respectively. We also investigate the magnetic properties by performing calculations of the antiferromagnetic spin structure factor, defined as the Fourier transform of the spin-spin correlation functions for f orbitals,

$$S_{ff}(\mathbf{q}) = \frac{1}{3N}\sum_{\mathbf{i},\mathbf{j}} e^{i\mathbf{q}\cdot(\mathbf{r}_i - \mathbf{r}_j)}\langle\vec{S}_{f\mathbf{i}} \cdot \vec{S}_{f\mathbf{j}}\rangle, \quad (5)$$

with $\mathbf{q} = (\pi, \pi, \pi)$. For singlet formation, we examine a correlator function:

$$C_{fd} = \frac{1}{3N}\sum_{\mathbf{i}}\langle\vec{S}_{f\mathbf{i}} \cdot \vec{S}_{d\mathbf{i}}\rangle. \quad (6)$$

Here, we define the fermionic spin operators as $\vec{S}_{f\mathbf{i}} = (f^\dagger_{\uparrow\mathbf{i}}\ f^\dagger_{\downarrow\mathbf{i}})\,\vec{\sigma}\,\begin{pmatrix} f_{\uparrow\mathbf{i}} \\ f_{\downarrow\mathbf{i}}\end{pmatrix}$, with $\vec{\sigma}$ being the Pauli spin matrices, while the $1/3$ factor in Eqs. (5) and (6) is for the average value along one spin component.

We extract the critical behavior by means of the antiferromagnetic correlation ratio

$$R_c(L) = 1 - \frac{S_{ff}(\mathbf{q}+\delta\mathbf{q})}{S_{ff}(\mathbf{q})}, \quad (7)$$

with $|\delta\mathbf{q}| = \frac{2\pi}{L}$. This is a renormalization-group invariant observable, in which the crossing points for different lattice sizes provide the critical points [29,30].

In addition to these equal-time correlation functions, we also calculate appropriate unequal-time quantities, including the magnetic susceptibility

$$\chi(\mathbf{q}) = \chi_{dd}(\mathbf{q}) + 2\chi_{df}(\mathbf{q}) + \chi_{ff}(\mathbf{q}), \quad (8)$$

with

$$\chi_{\alpha\gamma}(\mathbf{q}) = \frac{1}{3N}\sum_{\mathbf{i},\mathbf{j}}\int_0^\beta d\tau\,\langle\vec{S}_{\alpha,\mathbf{j}}(\tau) \cdot \vec{S}_{\gamma,\mathbf{i}}(0)\rangle e^{i\mathbf{q}\cdot(\mathbf{r}_i - \mathbf{r}_j)}, \quad (9)$$

($\alpha, \gamma = d$ or f), where we examine the uniform and staggered cases $\mathbf{q} = (0,0,0)$ and (π,π,π), respectively.

Finally, we also evaluate nuclear magnetic resonance (NMR) quantities, such as the time relaxation rate for the f electrons. For the low-frequency limit of the dynamic susceptibility, it is defined as (see, e.g., Ref. [31])

$$T^{-1}_{1,ff} = \gamma^2 k_B T \lim_{\omega\to 0}\sum_{\mathbf{q}} A^2(\mathbf{q})\,\frac{\chi''_{ff}(\mathbf{q},\gamma)}{\hbar\omega}, \quad (10)$$

where $A^2(\mathbf{q})$ is the square of the Fourier transform of the hyperfine interaction, and γ is the gyromagnetic ratio. The latter is related to the nuclear magnetic moment by $\gamma\hbar = g\mu_N\sqrt{I(I+1)}$, with μ_N being the nuclear magneton, g the nuclear g factor, and I the nuclear spin. $T_{1,ff}$ quantifies a characteristic time in which a component of the nuclear spin (of a given f orbital) reaches equilibrium after an external perturbation (magnetic field pulse). It is a dynamical (real-frequency) quantity whose numerical evaluation usually requires an analytic continuation of the imaginary-time DQMC data. Instead, we follow Ref. [32], which performs an approximation of this procedure, leading to

$$\frac{1}{T_1 T} = \frac{1}{\pi^2 T^2}\frac{\Gamma}{N}\sum_{\mathbf{i}}\langle S_{f,\mathbf{i}}(\tau=\beta/2)S_{f,\mathbf{i}}(0)\rangle, \qquad (11)$$

where $\Gamma \propto \gamma^2 A^2$ sets the energy.

III. RESULTS

A. Thermodynamic properties

We start our analysis by discussing the thermodynamic properties of the system—unless otherwise indicated, the following results are obtained for a 6×6×6 lattice (i.e., 216 sites with two orbitals per site). First, we investigate the internal energy, Eq. (3), displayed as a function of T/t in Fig. 1(a). The derivative of the internal energy with respect to the temperature yields the specific heat, Eq. (4), whose behavior should indicate the occurrence of phase transitions. Figure 1(b) displays $c\,(T)$ for $V/t = 1.4$, exhibiting a two-peak structure. Since numerical differentiation for a few data points is usually noisy, one may perform a nonlinear fit of the QMC energy points and differentiate the fitted curve, as shown by the dashed line in Fig. 1(b). Here we define such a fit on an exponential basis [33], by the function $e_{\rm fit}(T) = a_0 + \sum_{n=1}^{M} a_n \exp(-\beta n\Delta)$, with a cutoff in M (fixing $M \leqslant 10$ is enough). The agreement indicates the robustness of the fitting approach, which we repeat for other values of hybridization V/t, whose results are shown in Fig. 1(c).

There are several important features concerning the behavior of $c\,(T)$ to be emphasized. First, a high-temperature almost hybridization-independent peak at $T/t \sim 1.45$ is evident, which is due to the formation of local moments [33]. We also find a low-temperature peak, which is pushed to higher temperatures and decreases in intensity as V/t increases. This low-temperature peak is also seen for the two- and three-dimensional Hubbard models [11,33,34] and usually is associated with collective spin-wave excitations. In particular, for the three-dimensional Hubbard model, this low-temperature peak position signals the Néel temperature since the ground state is antiferromagnetic (AFM). For the 3D PAM, on the other hand, previous calculations for the specific heat were unable to resolve the low-T peak for values of V/t below the AFM-singlet quantum critical point [15,16], as we have done in this paper. As one expects a phase transition from the antiferromagnetic phase to the singlet phase, the position of the low-T peak may not uniquely identify the Néel temperature for the 3D PAM. Therefore, to probe whether the low-T peaks indicate the presence of long-range spin correlations, we next investigate the magnetic properties of the system.

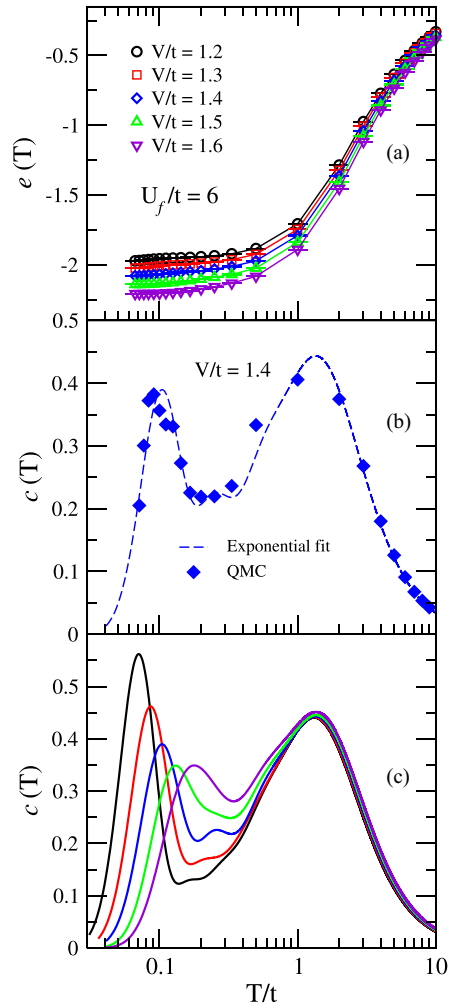

FIG. 1. (a) Energy as a function of temperature for different V/t, and (b) the specific heat as a function of the temperature for $V/t = 1.4$. Closed symbols represent data from numerical differentiation of the energy values, whereas the dashed line represents the differentiation of an exponential fit to the energy [33]. (c) Specific heat from the fit procedure for the same values of V/t as in panel (a). All data are for 6×6×6 lattices.

B. Magnetic properties

We proceed to examine the singlet correlator C_{fd}: a measure of the on-site spin-spin correlation between an f moment and the spin of a d electron. We find this quantity is always negative, pointing to antiferromagnetic coupling and singlet formation that increases in strength as V/t increases. As displayed in Fig. 2(a), C_{fd} has a rapid increase in modulus around $V/t \approx 1.3$, providing an initial indication of a change into a singlet phase.

In order to go beyond this rough indication from the singlet correlator, we also analyze the f-orbital AFM structure factor, Eq. (5), shown in Fig. 2(b). S_{ff} grows rapidly as V/t decreases from $V/t \sim 2$, especially for larger β, indicating the formation of long-range AFM order on the f orbitals as the singlet correlations diminish [Fig. 2(a)]. However, after reaching a maximum at $V/t \sim 1.3$, S_{ff} begins falling. Within the temperatures investigated, the structure factor as a function of V/t seems approximately symmetric around the maximum

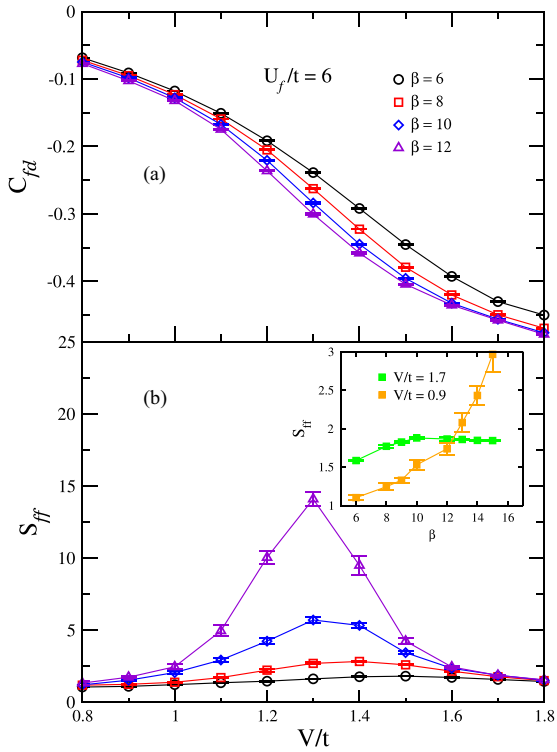

FIG. 2. (a) Singlet correlator and (b) antiferromagnetic structure factor as functions of the hybridization for different temperatures for 6×6×6 lattices. The inset in panel (b) shows the antiferromagnetic structure factor as a function of inverse temperature for hybridizations $V/t = 0.9$ and $V/t = 1.7$.

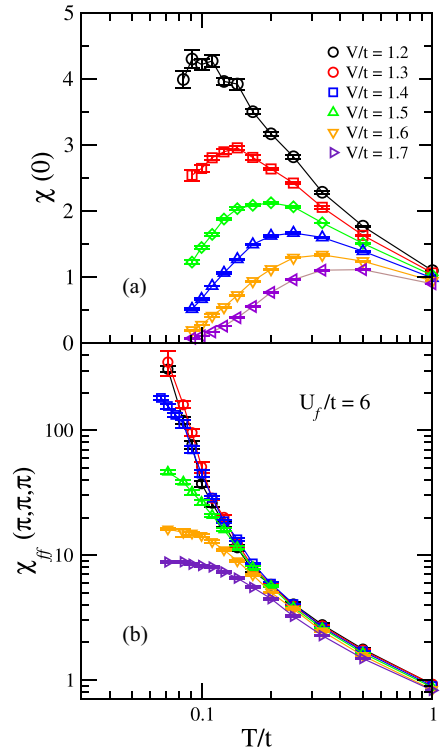

FIG. 3. Total uniform susceptibility (a) and staggered susceptibility in the f sites (b) for different values of V/t on 6×6×6 lattices.

in $V/t \approx 1.3$, but this is a high-temperature artifact. By further examining S_{ff} at lower T, e.g., for $V/t = 0.9$ and 1.7, as displayed in the inset of Fig. 2(b), one may notice that the responses for low and high V are quite different. Specifically, for $V/t = 0.9$, S_{ff} while seemingly small, grows very rapidly as β increases—see the inset of Fig. 2(b). This is in sharp contrast to the behavior at $V/t = 1.7$, where S_{ff} saturates at a small value as the temperature is lowered (increasing β). This, together with the fact that the singlet correlator is small for $V/t \sim 0.9$ suggests that the low-V/t region still has AFM order, but that the transition temperature T_N is below the smallest temperature-simulated $T_N < t/15$.

To further understand the magnetic behavior we turn to the uniform and staggered magnetic susceptibilities, shown in Figs. 3(a) and 3(b), respectively. For high temperatures, both uniform and staggered susceptibilities show the expected $1/T$ Curie behavior of free spins, while for low temperatures and small hybridizations (e.g., $V/t = 1.2$ and 1.3), the uniform susceptibility $\chi(0)$ displays a clear peak, followed by a strong suppression as T decreases. We recall that, in antiferromagnetic systems, such a maximum of $\chi(0)$ occurs at the Néel temperature. Here, as our system may exhibit AFM or singlet phases, and both exhibit a cusp for $\chi(0)$, one is not able to unambiguously identify T_N only from the response of the uniform susceptibility.

As is further discussed later, such a cusp in $\chi(0)$ occurs due to the emergence of the spin-singlet phase and gives the energy scale for the spin gap formation Δ_s. Such a gap in the spin excitations is clearly noticed when analyzing the staggered susceptibility, $\chi_{ff}(\pi, \pi, \pi)$, displayed in Fig. 3(b). In the thermodynamic limit, the staggered susceptibility should diverge at T_N, while $\chi_{ff}(\pi, \pi, \pi) \to 0$ in presence of a spin gap. Indeed, as shown in Fig. 3(b), the susceptibility displays a fast increase with decreasing T/t for $V/t \lesssim 1.4$, while it is strongly suppressed for larger hybridizations.

Early DQMC studies of two-dimensional PAM have shown evidence of a QCP at $V_c/t \approx 1.0$, separating an antiferromagnetically ordered ground state from a spin singlet [35]. The problem was recently revisited by DQMC and dynamical vertex approximation analyses, which show a similar value for the QCP [36,37]. One would expect that some finite-temperature quantities should reflect the characteristics of the different low-T phases, even for the 2D case (where the occurrence of long-range-ordered AFM phase is forbidden at finite temperatures). Indeed, this is the case of NMR measurements, in particular, the spin-lattice relaxation rate, Eq. (10), which may signal the existence of a spin gap [38]. Previous DQMC studies of the 2D PAM have shown that, at the critical point V_c, the $1/T_1T$ is almost constant at low temperatures, while increasing (reducing) for $V < V_c$ ($V > V_c$) [39]. Figure 4 displays the behavior of the relaxation rate as a function of temperature for different values of V/t, for the 3D PAM (linear size $L = 6$). Notice that, within the AFM phase ($V/t = 1.2$ or 1.3) $1/T_1T$ approaches a finite nonzero value as $T/t \to 0$, consistent with the absence of a spin gap, i.e., the presence of spin-wave excitations. On the other hand, for larger V, $1/T_1T$ decreases monotonically when T is lowered, reflecting a spin-gapped ground state. Interestingly, the change in behavior of $1/T_1T$ occurs around $V/t \sim 1.4$, where both results

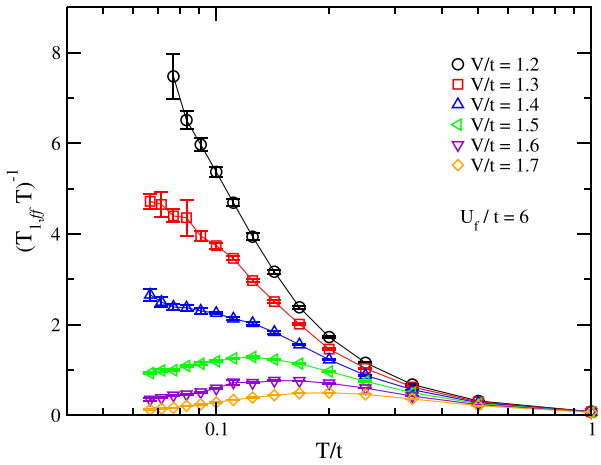

FIG. 4. Spin-lattice relaxation rate of the 3D PAM as a function of temperature, for different hybridizations and 6×6×6 lattices.

from specific heat and susceptibilities support the disappearance of AFM order.

In order to estimate and track the spin-gap Δ_s opening, it is useful to analyze the unequal-time spin-spin correlation functions $C(\mathbf{i}, \mathbf{j}, \tau) = \langle S^z_{\mathbf{j}}(\tau) S^z_{\mathbf{i}}(0)\rangle$. In particular, in the presence of a spin gap, the asymptotic behavior of the unequal-time staggered structure factor, $C(\mathbf{q}, \tau) = \frac{1}{N}\sum_{\mathbf{r}_{ij}} e^{-i\mathbf{q}\mathbf{r}_{ij}} C(\mathbf{i} = 0, \mathbf{j}, \tau)$, with $\mathbf{q} = (\pi, \pi)$, and $\mathbf{r}_{ij} = \mathbf{i} - \mathbf{j}\mathbf{r}$, becomes

$$\lim_{\tau\to\infty} C(\mathbf{q}, \tau) \propto \exp(-\Delta_s \tau), \tag{12}$$

from which one is able to estimate the spin gap by an exponential fitting. From this procedure, we obtain Δ_s as a function of V/t, and T/t, as exhibited in Fig. 5(a). For large hybridization values, we notice that the gap increases with decreasing temperature, remaining finite at low T. For small hybridizations, on the other hand, the gap is small and decreases with decreasing temperature; that is, one has a spin gapless phase, in line with our previous expectation of AFM order. The change in such behavior occurs for $V/t \approx 1.5$, where the spin gap is temperature independent. In order to further examine the gap opening, it is important to analyze Δ_s in the ground state. To this end, we perform least-squares polynomial fits to extrapolate $\Delta_s(V, T) \to \Delta_s(V, 0)$, as shown in Fig. 5(b). In particular, for $V_c/t = 1.45 \pm 0.05$, we obtain a vanishing gap at the ground state; i.e., we have a QCP separating an AFM phase at low hybridization from a (singlet) Kondo phase at large V/t.

Although we have estimated the location of the QCP, the Néel temperatures (for $V < V_c$) are ill-defined by the specific heat and homogeneous susceptibility behavior. A thorough probe of T_N is provided by a finite-size scaling analysis of the correlation ratio, Eq. (7), a renormalization-group invariant, and shown in Fig. 6 as a function of temperature, for different hybridizations and system sizes. The crossing of $R_c(L)$ for different lattice sizes provides the critical temperatures, which are $T_N/t \simeq 0.08$–0.10 for the range of $V/t = 1.1$–1.4. For larger hybridizations, e.g., for $V/t = 1.6$, no crossing is expected and thus there is no long-range order. The behavior for $V/t = 1.5$ is subtle: the curves become closer as the temperature is lowered, but they do not cross within the range we

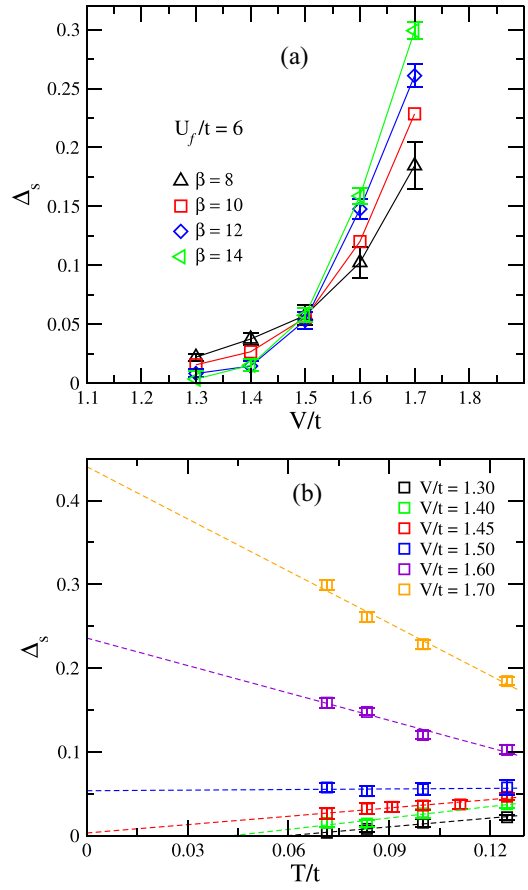

FIG. 5. The spin gap Δ_s (a) as a function of hybridization for different inverse temperatures and (b) as a function of the temperature for different hybridizations. The ground-state vanishing gap occurs for $V_c/t = 1.45 \pm 0.05$.

analyzed. It may indicate that (i) the crossing would occur at very low T or (ii) the curves may not cross, even at $T = 0$. While the former option is possible, the latter is more likely. We recall that $R_c \to 1$ (for $T = 0$ and $L \to \infty$) when long-range order occurs [40]; however, R_c seems to converge for a smaller value, for $V/t = 1.5$, which suggests the absence of magnetism.

Since the correlation ratio shows no abrupt features, the paramagnetic metallic to antiferromagnetic insulator finite-temperature phase transition is more likely to be continuous. However, a remark should be made concerning the quantum phase transition: as the Néel temperatures do not decrease close to V_c/t, this may indicate a first-order transition from the AFM phase to the Kondo singlet one or, at least, a very sharp continuous transition. Since first-order transitions are challenging to determine by Monte Carlo methods, the nature of the phase transition that occurs at the ground state remains an open question for the 3D PAM. By the same token, for smaller hybridizations, T_N will decrease, as previously discussed in the context of Fig. 2(b). Going to such low T/t is hard to achieve in three-dimensional geometries. It is worth noting that this computational limitation also affects the determination of T_N in the 3D single-band Hubbard model, where $T_N \sim te^{-a\sqrt{t/U}}$ is very small at weak coupling [9,10,12,41–43].

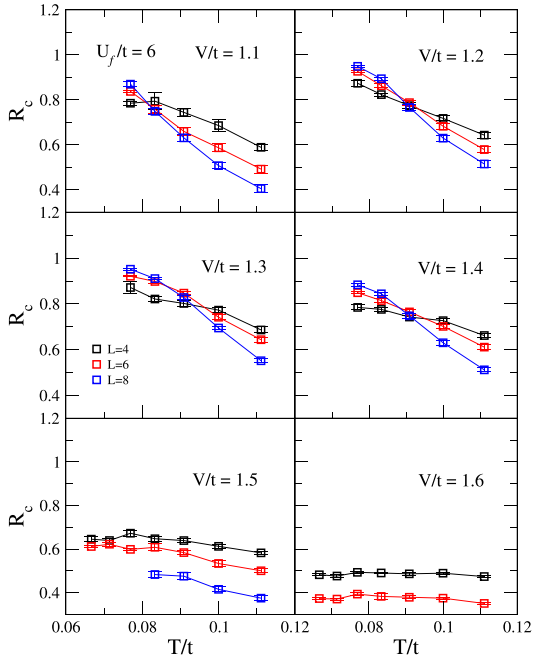

FIG. 6. Determinant quantum Monte Carlo results for the AF correlation ratio, as a function of temperature, for different lattice sizes and hybridizations, at fixed $U_f/t = 6$. The crossing points separate the paramagnetic phase and the Néel phases.

We conclude by comparing the energy scales of our results with those from the literature. Early QMC attempts to investigate the three-dimensional PAM were performed in Refs. [15–17], providing hints that such an AFM long-range order requires very low temperatures to be achieved. By "low-temperature" we mean by comparison with the 3D Hubbard model [11,44,45], whose maximum of the Néel temperature is $T_N/t \approx 0.33$ and occurs at $U_f/t \approx 8$. Here, we provide T_N for the 3D PAM, showing that these energy scales are indeed much lower than those from the Hubbard model [46]. This difference is expected due to the weak indirect coupling between f electrons mediated by conduction ones—first addressed by DMFT studies [47]. In view of this, it is expected that the value of V_c/t should change for different values of U_f, but the maxima of T_N should keep values similar to those presented for $U_f/t = 6$.

C. Transport properties

In the ground state, the AFM and singlet phases are both insulators. However, at finite temperatures, a crossover from a metallic to an insulating behavior should occur at an appropriate energy scale. Therefore, as a complementary study, we also probe such a crossover as the temperature is lowered, showing that its features can be identified from the behavior of thermodynamic quantities [48].

We first examine the c electrons' kinetic energy per particle,

$$\langle K\rangle = -\frac{t}{N}\left\langle \sum_{\langle \mathbf{i},\mathbf{j}\rangle,\sigma} (d^{\dagger}_{\mathbf{i},\sigma} d_{\mathbf{j},\sigma} + \text{H.c.})\right\rangle, \tag{13}$$

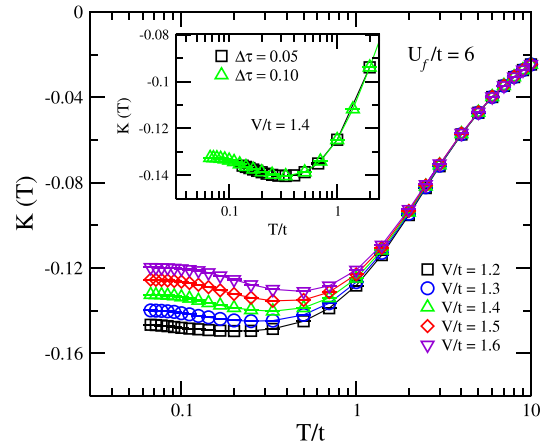

FIG. 7. Kinetic energy K as a function of temperature for different values of V/t for 6×6×6 lattices. The inset shows K as a function of T/t for $V/t = 1.4$ and two different values of imaginary-time discretization: $\Delta\tau = 0.05$ (squares) and $\Delta\tau = 0.10$ (triangles).

whose behavior is presented in Fig. 7 as a function of temperature, for different values of hybridization. For all hybridization values, the following behavior is noticed: at high temperatures, $\langle K\rangle$ is reduced as temperature is lowered, reaching a minimum for a given energy scale $T_{\min(\langle K\rangle)}$ and, therefore, increasing as $T \to 0$ when $T < T_{\min(\langle K\rangle)}$. The sign change in $\frac{\partial\langle K\rangle}{\partial T}$, from positive to negative, is consistent with an evolution from metallic to insulator behavior, respectively [48]. For a metallic system, the kinetic energy should reduce as the temperature is lowered ($\partial\langle K\rangle/\partial T > 0$); however, when a charge gap opens, the higher-energy states are less likely populated, which may cease the decreasing of $\langle K\rangle$, or even increase it ($\partial\langle K\rangle/\partial T < 0$), as exhibited in Fig. 7. In order to emphasize the absence of imaginary-time discretization errors, the inset in Fig. 7 shows the kinetic energy per particle for $V/t = 1.4$ as a function of temperature for two different values of $\Delta\tau$, from which is clear that our choice of $\Delta\tau$ does not affect the results of $\langle K\rangle$.

Notice that, while this result suggests an insulator for $T < T_{\min(\langle K\rangle)}$, it contrasts with our expectation for the behavior of the homogeneous susceptibility in Fig. 3. When both charge and spin gaps are opened (e.g., for band insulators), we must have $\partial\chi(0)/\partial T > 0$ below temperatures that lead to the insulating state. That is, the positive derivative indicates that the spin gap is reducing its size due to thermal fluctuations, facilitating the spin response to external fields. However, as shown in Fig. 3, such behavior occurs at $T_{\max(\chi)} \neq T_{\min(\langle K\rangle)}$: there is a large region where $\frac{\partial}{\partial T}\chi(0) \leqslant 0$, consistent with a Pauli metal for d electrons + local moment Curie behavior for f electrons, while ($\frac{\partial\langle K\rangle}{\partial T} < 0$), suggesting an insulator. Such an unconventional insulating phase is related to non-Fermi liquid behavior for this region [48], and here is defined as a bad metal phase.

To further emphasize this bad metallic phase, we also investigate the dc conductivity,

$$\sigma_{\text{dc}} = \frac{\beta^2}{\pi}\Lambda_{xx}(\mathbf{q} = \mathbf{0}, \tau = \beta/2), \tag{14}$$

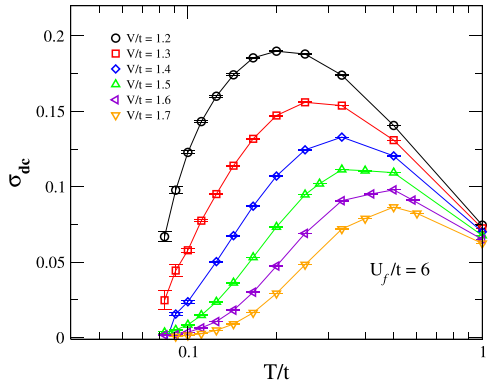

FIG. 8. dc conductivity as a function of the temperature, for different values of V/t and 6×6×6 lattices.

in which

$$\Lambda_{xx}(\mathbf{q},\tau) = \langle j_x(\mathbf{q},\tau) j_x(-\mathbf{q},0)\rangle, \tag{15}$$

with $j_x(\mathbf{q},\tau)$ being the Fourier transform of

$$j_x(\mathbf{i},\tau) = e^{\tau\mathcal{H}}\left[it \sum_{\sigma} (d^{\dagger}_{\mathbf{i}+\mathbf{x}\sigma} d_{\mathbf{i}\sigma} - d^{\dagger}_{\mathbf{i}\sigma} d_{\mathbf{i}+\mathbf{x}\sigma}) \right] e^{-\tau\mathcal{H}} \tag{16}$$

(see, e.g., Refs. [49–51]). The behavior of $\sigma_{\rm dc}$ as a function of temperature is displayed in Fig. 8, which shows $\sigma_{\rm dc} \to 0$ as $T \to 0$ for all V/t, consistent with an insulating phase ground state for the entire range of hybridizations. However, this insulating feature—i.e., $\frac{\partial \sigma_{\rm dc}}{\partial T} > 0$—changes depending on the temperature, with $\sigma_{\rm dc}$ exhibiting a maximum at $T_{\max(\sigma_{\rm dc})}$. Interestingly, the values of $T_{\max(\sigma_{\rm dc})}$ are consistent with $T_{\min(\langle K\rangle)}$, both signaling a crossover into a bad metallic phase.

IV. CONCLUSIONS

In this work, we have investigated the thermodynamic, magnetic, and transport properties of the three-dimensional periodic Anderson model through unbiased DQMC simulations. For the thermodynamic properties, we examined the specific heat for different hybridizations. We find a broad, high-temperature peak that is independent of V/t, while the low-T peak, on the other hand, is strongly V dependent. This low-T peak is associated with the emergence of the AFM phase for $V < V_c$. However, it does not give precise information about the singlet phase for $V > V_c$ [52].

To get more quantitative insight into the singlet formation, we investigated the AFM structure factor and the correlator function for different V/t and temperatures. In particular, the AFM structure factor pointed out the energy scale for the quantum critical point. This quantum phase transition between an AFM state and a singlet state was obtained by analyzing the spin gap, the NMR time relaxation rate, and the staggered magnetic susceptibility, which agree with $V_c/t = 1.45 \pm 0.05$. The Néel temperature within the AFM phase was probed by the antiferromagnetic correlation ratio and lies in the range $T/t \simeq 0.08$–0.10 for all V/t investigated. Finally, by investigating the transport properties, we find out that there is a region in which the system behaves as a bad metal; i.e., it presents insulator features for the kinetic energy (namely, $\frac{\partial \langle K\rangle}{\partial T} < 0$), while keeping metallic ones for the homogeneous susceptibility (namely, $\frac{\partial \chi}{\partial T} \leqslant 0$—a Pauli metal for d electrons + local moment Curie behavior for f ones).

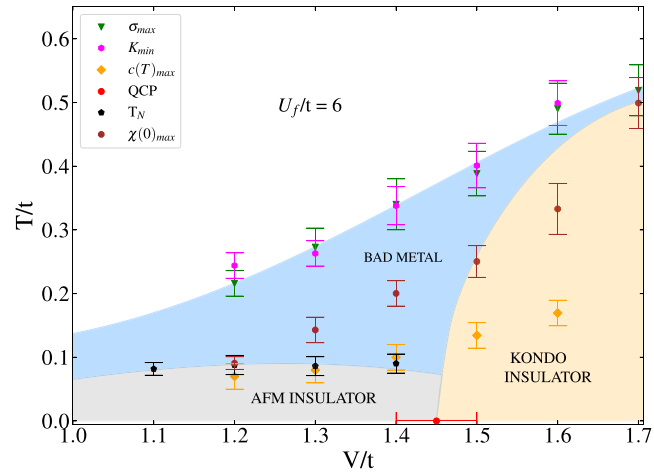

FIG. 9. Energy scales for the three-dimensional periodic Anderson model for different values of V/t; the curves and color maps are guides to the eye. For comparison, the Néel temperature T_N of the 3D Hubbard model, when plotted versus on-site interaction U_f/t, exhibits a broad maximum with $T_N/t \sim 0.3$ in the range $6 \lesssim U_f/t \lesssim 10$.

In summary, our work presents detailed finite-temperature results for the three-dimensional periodic Anderson model in a simple cubic lattice, allowing the quantitative determination of different energy scales. Our key findings are given in Fig. 9, which presents these energy scales and the resulting finite-temperature phase diagram. In particular, we show (i) the quantum critical point, QCP; (ii) the temperature of the maxima for the homogeneous susceptibility, $\chi(0)_{\rm max}$; (iii) the minima for the d electrons' hopping energy, $K_{\rm min}$; (iv) the temperature of the maxima of the conductivity $\sigma_{\rm max}$; (v) the low-temperature-specific heat peak position, $c(T)_{\rm max}$; and finally (vi) the Néel temperatures T_N obtained from a finite-size scaling analysis. Knowing precise values for these energy scales at half-filling is an essential step towards examining other more complex facets of this model which emerge with doping, including the occurrence of d-wave superconductivity due to frustration effects [53] or the enhancement of magnetism due to depletion [54–56]. Indeed, Fig. 9 provides detailed data for the PAM across an interesting part of its phase diagram encompassing the AFM-singlet QCP, which may help guide future theoretical and experimental work on heavy-fermion materials. Other interesting questions, including the formation of the heavy-fermion state and how large V/t may affect the high-T specific heat peak (and, consequently, the local moment formation), will be investigated in the near future.

ACKNOWLEDGMENTS

We thank E. C. Andrade for useful suggestions concerning the manuscript. The authors are grateful to the Brazilian Agencies Conselho Nacional de Desenvolvimento Científico e Tecnológico (CNPq), Coordenação de Aperfeiçoamento

de Pessoal de Ensino Superior (CAPES), Fundação Carlos Chagas de Apoio à Pesquisa do Estado do Rio de Janeiro (FAPERJ), and Instituto Nacional de Ciência e Tecnologia de Informação Quântica (INCT-IQ) for funding this project. N.C.C. acknowledges financial support from CNPq, Grant No. 313065/2021-7, and from FAPERJ—Fundação Carlos Chagas Filho de Amparo à Pesquisa do Estado do Rio de Janeiro—, Grant No. 200.258/2023 (SEI-260003/000623/2023). T.P. acknowledges financial support from CNPq Grants No. 403130/2021-2 and No. 308335/2019-8, and FAPERJ Grants No. E-26/200.959/2022 and No. E-26/210.100/2023. The work of R.S. was supported by the Grant No. DE-SC-0014671, funded by the U.S. Department of Energy, Office of Science, Basic Energy Sciences. N.C.C. was responsible for the concept of the project. W.S.O. did the primary data collection and analysis. All authors participated in obtaining the data, interpreting of results, and writing the manuscript.

[1] M. Raczkowski, R. Peters, T. T. Phùng, N. Takemori, F. F. Assaad, A. Honecker, and J. Vahedi, Hubbard model on the honeycomb lattice: From static and dynamical mean-field theories to lattice quantum Monte Carlo simulations, Phys. Rev. B **101**, 125103 (2020).

[2] G. Paleari, F. Hébert, B. Cohen-Stead, K. Barros, R. T. Scalettar, and G. G. Batrouni, Quantum Monte Carlo study of an anharmonic Holstein model, Phys. Rev. B **103**, 195117 (2021).

[3] B. Xing, W.-T. Chiu, D. Poletti, R. T. Scalettar, and G. Batrouni, Quantum Monte Carlo Simulations of the 2D Su-Schrieffer-Heeger Model, Phys. Rev. Lett. **126**, 017601 (2021).

[4] D. Hu, J.-J. Dong, and Y.-F. Yang, Hybridization fluctuations in the half-filled periodic Anderson model, Phys. Rev. B **100**, 195133 (2019).

[5] D. J. Scalapino, A common thread: The pairing interaction for unconventional superconductors, Rev. Mod. Phys. **84**, 1383 (2012).

[6] V. N. Kotov, B. Uchoa, V. M. Pereira, F. Guinea, and A. H. Castro Neto, Electron-electron interactions in graphene: Current status and perspectives, Rev. Mod. Phys. **84**, 1067 (2012).

[7] S. Manzeli, D. Ovchinnikov, D. Pasquier, O.V. Yazyev, and A. Kis, 2D transition metal dichalcogenides, Nat. Rev. Mater. **2**, 17033 (2017).

[8] The reduced (Ising) order parameter symmetry of the Holstein case does support a finite T transition in 2D.

[9] J. E. Hirsch, Simulations of the three-dimensional Hubbard model: Half-filled band sector, Phys. Rev. B **35**, 1851 (1987).

[10] R. T. Scalettar, D. J. Scalapino, R. L. Sugar, and D. Toussaint, Phase diagram of the half-filled 3D Hubbard model, Phys. Rev. B **39**, 4711 (1989).

[11] R Staudt, M. Dzierzawa, and A. Muramatsu, Phase diagram of the three-dimensional Hubbard model at half filling, Eur. Phys. J. B **17**, 411 (2000).

[12] S. Fuchs, E. Gull, L. Pollet, E. Burovski, E. Kozik, T. Pruschke, and M. Troyer, Thermodynamics of the 3D Hubbard Model on Approaching the Néel Transition, Phys. Rev. Lett. **106**, 030401 (2011).

[13] B. Cohen-Stead, K. Barros, Z. Y. Meng, C. Chen, R. T. Scalettar, and G. G. Batrouni, Langevin simulations of the half-filled cubic Holstein model, Phys. Rev. B **102**, 161108(R) (2020).

[14] B. Cohen-Stead, K. Barros, R. Scalettar, and S. Johnston, A hybrid Monte Carlo study of bond-stretching electron–phonon interactions and charge order in $BaBiO_3$, npj Compu. Mater. **9**, 40 (2023).

[15] A.K. McMahan, C. Huscroft, R.T. Scalettar, and E.L. Pollock, Volume-collapse transitions in the rare earth metals, J. Comput.-Aided Mater. Des. **5**, 131 (1998).

[16] C. Huscroft, A. K. McMahan, and R. T. Scalettar, Magnetic and Thermodynamic Properties of the Three-Dimensional Periodic Anderson Hamiltonian, Phys. Rev. Lett. **82**, 2342 (1999).

[17] T. Paiva, G. Esirgen, R. T. Scalettar, C. Huscroft, and A. K. McMahan, Doping-dependent study of the periodic Anderson model in three dimensions, Phys. Rev. B **68**, 195111 (2003).

[18] B. H. Bernhard and C. Lacroix, Thermodynamics of the Anderson lattice, Phys. Rev. B **60**, 12149 (1999).

[19] K. Held, A. K. McMahan, and R. T. Scalettar, Cerium Volume Collapse: Results from the Merger of Dynamical Mean-Field Theory and Local Density Approximation, Phys. Rev. Lett. **87**, 276404 (2001).

[20] R. Blankenbecler, D. J. Scalapino, and R. L. Sugar, Monte Carlo calculations of coupled boson-fermion systems. I, Phys. Rev. D **24**, 2278 (1981).

[21] J. E. Hirsch, Two-dimensional Hubbard model: Numerical simulation study, Phys. Rev. B **31**, 4403 (1985).

[22] S. R. White, D. J. Scalapino, R. L. Sugar, E. Y. Loh, J. E. Gubernatis, and R. T. Scalettar, Numerical study of the two-dimensional Hubbard model, Phys. Rev. B **40**, 506 (1989).

[23] R. R. dos Santos, Introduction to quantum Monte Carlo simulations for fermionic systems, Braz. J. Phys. **33**, 36 (2003).

[24] J. Gubernatis, N. Kawashima, and P. Werner, *Quantum Monte Carlo Methods: Algorithms for Lattice Models* (Cambridge University Press, Cambridge, England, 2016).

[25] F. Becca and S. Sorella, *Quantum Monte Carlo Approaches for Correlated Systems* (Cambridge University Press, Cambridge, England, 2017).

[26] E. Y. Loh, J. E. Gubernatis, R. T. Scalettar, S. R. White, D. J. Scalapino, and R. L. Sugar, Sign problem in the numerical simulation of many-electron systems, Phys. Rev. B **41**, 9301 (1990).

[27] M. Troyer and U.-J. Wiese, Computational Complexity and Fundamental Limitations to Fermionic Quantum Monte Carlo Simulations, Phys. Rev. Lett. **94**, 170201 (2005).

[28] R. Mondaini, S. Tarat, and R. T. Scalettar, Quantum critical points and the sign problem, Science **375**, 418 (2022).

[29] R. K. Kaul, Spin Nematics, Valence-Bond Solids, and Spin Liquids in SO(N) Quantum Spin Models on the Triangular Lattice, Phys. Rev. Lett. **115**, 157202 (2015).

[30] A. S. Darmawan, Y. Nomura, Y. Yamaji, and M. Imada, Stripe and superconducting order competing in the Hubbard model on a square lattice studied by a combined variational Monte Carlo and tensor network method, Phys. Rev. B **98**, 205132 (2018).

[31] N.J. Curro, Nuclear magnetic resonance in the heavy fermion superconductors, Rep. Prog. Phys. **72**, 026502 (2009).

[32] M. Randeria, N. Trivedi, A. Moreo, and R. T. Scalettar, Pairing and Spin Gap in the Normal State of Short Coherence Length Superconductors, Phys. Rev. Lett. **69**, 2001 (1992).
[33] T. Paiva, R. T. Scalettar, C. Huscroft, and A. K. McMahan, Signatures of spin and charge energy scales in the local moment and specific heat of the half-filled two-dimensional Hubbard model, Phys. Rev. B **63**, 125116 (2001).
[34] D. Duffy and A. Moreo, Specific heat of the two-dimensional Hubbard model, Phys. Rev. B **55**, 12918 (1997).
[35] M. Vekić, J. W. Cannon, D. J. Scalapino, R. T. Scalettar, and R. L. Sugar, Competition between Antiferromagnetic Order and Spin-Liquid Behavior in the Two-Dimensional Periodic Anderson Model at Half Filling, Phys. Rev. Lett. **74**, 2367 (1995).
[36] W. Hu, R. T. Scalettar, E. W. Huang, and B. Moritz, Effects of an additional conduction band on the singlet-antiferromagnet competition in the periodic Anderson model, Phys. Rev. B **95**, 235122 (2017).
[37] T. Schäfer, A. A. Katanin, M. Kitatani, A. Toschi, and K. Held, Quantum Criticality in the Two-Dimensional Periodic Anderson Model, Phys. Rev. Lett. **122**, 227201 (2019).
[38] T. Mendes-Santos, N. C. Costa, G. Batrouni, N. Curro, R. R. dos Santos, T. Paiva, and R. T. Scalettar, Impurities near an antiferromagnetic-singlet quantum critical point, Phys. Rev. B **95**, 054419 (2017).
[39] N. C. Costa, T. Mendes-Santos, T. Paiva, N. J. Curro, R. R. dos Santos, and R. T. Scalettar, Coherence temperature in the diluted periodic Anderson model, Phys. Rev. B **99**, 195116 (2019).
[40] M. Hohenadler and G. G. Batrouni, Dominant charge density wave correlations in the Holstein model on the half-filled square lattice, Phys. Rev. B **100**, 165114 (2019).
[41] J.C. Slater, Magnetic effects and the Hartree-Fock equation, Phys. Rev. **82**, 538 (1951).
[42] N. Nagaosa, *Quantum Field Theory in Strongly Correlated Electronic Systems* (Springer, Berlin, 1999).
[43] E. Kozik, E. Burovski, V. W. Scarola, and M. Troyer, Néel temperature and thermodynamics of the half-filled three-dimensional Hubbard model by diagrammatic determinant Monte Carlo, Phys. Rev. B **87**, 205102 (2013).
[44] D. Hirschmeier, H. Hafermann, E. Gull, A. I. Lichtenstein, and A. E. Antipov, Mechanisms of finite-temperature magnetism in the three-dimensional Hubbard model, Phys. Rev. B **92**, 144409 (2015).
[45] E. Khatami, Three-dimensional Hubbard model in the thermodynamic limit, Phys. Rev. B **94**, 125114 (2016).
[46] Interestingly, the Néel temperatures obtained by DMFT [37,47] are compatible with our QMC ones.
[47] K. Held, C. Huscroft, R. T. Scalettar, and A. K. McMahan, Similarities between the Hubbard and Periodic Anderson Models at Finite Temperatures, Phys. Rev. Lett. **85**, 373 (2000).
[48] A. J. Kim, F. Simkovic, and E. Kozik, Spin and Charge Correlations across the Metal-to-Insulator Crossover in the Half-Filled 2D Hubbard Model, Phys. Rev. Lett. **124**, 117602 (2020).
[49] N. Trivedi, R. T. Scalettar, and M. Randeria, Superconductor-insulator transition in a disordered electronic system, Phys. Rev. B **54**, R3756 (1996).
[50] P. J. H. Denteneer, R. T. Scalettar, and N. Trivedi, Conducting Phase in the Two-Dimensional Disordered Hubbard Model, Phys. Rev. Lett. **83**, 4610 (1999).
[51] R. Mondaini, K. Bouadim, T. Paiva, and R. R. dos Santos, Finite-size effects in transport data from quantum Monte Carlo simulations, Phys. Rev. B **85**, 125127 (2012).
[52] We expect that, for $L \to \infty$, the low-T peak would diverge for $V < V_c$, due to the AFM phase transition, while it becomes just a cusp for $V > V_c$.
[53] W. Wu and A.-M.-S. Tremblay, d-Wave Superconductivity in the Frustrated Two-Dimensional Periodic Anderson Model, Phys. Rev. X **5**, 011019 (2015).
[54] F. F. Assaad, Depleted Kondo lattices: Quantum Monte Carlo and mean-field calculations, Phys. Rev. B **65**, 115104 (2002).
[55] N. C. Costa, M. V. Araújo, J. P. Lima, T. Paiva, R. R. dos Santos, and R. T. Scalettar, Compressible ferrimagnetism in the depleted periodic Anderson model, Phys. Rev. B **97**, 085123 (2018).
[56] M. Jiang, Enhanced tendency towards d-wave pairing and antiferromagnetism in a doped staggered periodic Anderson model, Phys. Rev. B **102**, 085119 (2020).